Supplementary Information for:

Early maximum extent of paleoglaciers from Mediterranean mountains during the last glaciation

D. Domínguez-Villar, R.M. Carrasco, J. Pedraza,
H. Cheng, R.L. Edwards, J.K. Willenbring

Correspondence and request for materials should be addressed to D.D.V.

Supplementary Information

The maximum extent of paleoglaciers in central Spain and its sampling for ^{10}Be dating

The maximum extent of glaciation in the mountains from central Spain was considered to be a large moraine system formed by the most continuous and longer lateral moraines (the frontal moraines are rarely preserved) that extends along the edges of the ablation zones of most of the paleoglacier valleys[1,2]. This geomorphic unit is recognized along the different massifs and is called the Principal Moraine (PM). However, detailed geomorphologic mapping of glacier deposits has revealed that their extent exceeded the limit of the PM as shown by little moraines, boulder-belts and/or erratic strewn boulders. This unit, called Peripheral Deposits (PD), has been broadly recognized along the different massifs and its most external geomorphic features are considered the Glacial Maximum Extent (GME) of the region[3]. The PD and PM units are contiguous, which prevented the broad identification of the former unit until detailed geomorphic maps were available. Thus, in most cases PD cannot be recognized in the lateral moraine complexes because of the moraine distortion after glacier melt out due to the steep slopes of the valleys. However, the morphostructure of the summits in the Central Iberian System is characterized by the tectonic dislocation of a pre-Quaternary erosive surface that forms plateaus and shelves at different altitudes[4]. Thus, the areal distribution of elevations shows frequent relatively flat surfaces at the altitude where moraines were deposited during the GME stage: around 1400 to 1900 m asl (Fig. S1). The limited slope in these locations has favoured the preservation of the original morphology of the paleoglaciers extent during different stages, allowing a clear differentiation of MP and PD units. The external limits of both units are close in space (<100-500 m), and PM frequently overrides in part the PD, especially when PM is very large in comparison with PD. Nevertheless, the overlapping of these geomorphic units responds to local glacier dynamics and the PM clearly represents a regional stage with smaller areal extent than the PD. The identification of geomorphic features predating the last glaciation (e.g., flared slopes or heavily weathered boulders) in contact with the external edge of the PD indicates that the glaciers reach their GME while depositing external geomorphic features of the PD.

We chose to date certain boulders by *in situ*-produced cosmogenic ^{10}Be exposure dating if they showed signs of glacier abrasion, limited apparent weathering after deposition and no signs of rotation since original placement. As the glaciers of these mountains frequently produced large boulders, we only considered samples that were boulders standing 1 to 5 m from the surface, showed evidence of glacial erosion, were situated just on the crest of a moraine if they were not erratic boulders, and were found 'in place' in a stable position with no signs of rotation. These sampling criteria limited the possibilities of the boulders to retain a ^{10}Be inheritance from pre-exposure or to have been previously buried or tilted/rolled due to sediment erosion at its base. Additionally, boulders with heavy signs of post-depositional weathering were avoided, minimizing the lost of material due to erosion at the rock surface. Boulders that did not fit these criteria were not sampled, which implies that the most external boulders of each glacier were not always sampled even if they were identified. Boulders from different geomorphic features of the PD (i.e., moraines, boulders-belts or erratic boulders) were sampled. When possible at least two samples were taken in each geomorphic feature.

The most external geomorphic features of the PD are frequently erratic boulders. The scattered distribution of these boulders illustrates the scarce sedimentologic record available for the GME, especially considering the narrow fringe for these elements to occur within the PD unit along the edges of the paleoglacier (i.e., tens of metres). Therefore, even if the most external recognized geomorphic features have been sampled in all the surveyed glaciers, there is an inherent risk for the GME to lack a geomorphic record in the studied sequence (i.e., the most external geomorphic features identified could not represent the GME of the paleoglacier). Alternatively, geomorphic features from the GME could have been lost with time or have doubtful signs of glaciation, in which case they were not considered in this research. A statistical approach was considered to minimize this factor by surveying several sequences from different massifs. Thus, the combination of samples from different paleoglaciers is used to provide a statistically representative age for the paleoglacier stages in the region assuming that paleoclimate and not local factors dominated the extent of the glaciers.

Interpretation of $\delta^{18}O$ record from Eagle Cave stalagmites

The $\delta^{18}O$ and $\delta^{13}C$ isotope values of the carbonate speleothems EA1 and EA4 along the growth axis of both stalagmites have a poor correlation (r^2=0.07 in both cases). Additionally, two profiles along single laminas in EA-4 speleothem (EA1 is too thin and does not have discernible laminas) show no correlation at 90% confidence interval (p-values >0.1) and there is no significant increase of $\delta^{18}O$ aside from the centre of the speleothem. These data support that kinetic fractionation was close to equilibrium conditions[5] and does not control the variability of the stable isotope signal in these speleothems. However, the $\delta^{18}O$ record from Eagle Cave stalagmites depends on several factors (i.e., temperature, amount of rainfall, seasonality of rainfall, source of moisture, seawater $\delta^{18}O$ composition and mineralogy). Nevertheless, quantification of the impact of some of these controls allows the evaluation of their impact in the recorded signal.

The monthly rainfall $\delta^{18}O$ values at Eagle Cave, collected from 2009 to 2011, are positively correlated with temperature 0.23 ‰/ºC (r^2=0.42, p-value <0.01, n=30), although this thermal dependence is counteracted with the fractionation during calcite/aragonite precipitation, which magnitude range from -0.21 to -0.24‰ºC between 0 and 20 ºC[6,7]. Any possible misbalance between these two gradients falls within carbonate analytical uncertainties (0.1 ‰). Therefore, temperature should not impact the $\delta^{18}O$ record significantly, which is confirmed by the speleothems isotope signal. During the relatively warm Early Holocene isotope values have some of the lowest values, whereas high isotope values are achieved during the extreme cold Heinrich events H2 and H3 in Iberia[8,9].

A relationship of -1.64‰/100 mm exists between monthly amount of rainfall and its $\delta^{18}O$ values (r^2=0.33, p-value <0.01, n=30). However, a more pronounced isotopic gradient of -4.15‰/100 mm (r^2=0.39, p-value <0.01, n=25) is achieved when the months with rainfall over 150 mm are excluded (above this threshold the isotope ratio does not respond to amount of rainfall, probably indicating the exhaustion of the rainfall storage, preventing further Rayleigh distillation). The inter-annual relationship of amount of rainfall and its oxygen isotope ratio provides a more realistic gradient of -0.29‰/100 mm (r^2=0.99, p<0.01, n=3), although the short time series makes this number tentative. In any case, these gradients show that changes in amount of rainfall could explain >1‰ variability in the $\delta^{18}O$ record. The low $\delta^{18}O$ values during the Early

Holocene in comparison with the glacial period agree with the expected impact of amount of rainfall on $\delta^{18}O$ values due to wetter conditions after the glaciation[8,9]. The control of amount of rainfall in the recorded isotope ratio is also supported by the highest $\delta^{18}O$ values recorded during Heinrich events H2 and H3, which were extremely dry in the Peninsula[8,9].

Seasonality in the monthly rainfall oxygen isotope ratio is on the order of 8‰ at Eagle Cave. Thus, lower $\delta^{18}O$ values in the karst aquifer recharge should be expected with increased winter precipitation and vice versa. The impact of this factor in available isotope rainfall data is difficult to evaluate due to the short time series, but available data show no significant correlation (at 90% of confidence interval) between annual isotope ratios and percentage of winter precipitation (JFM). Additionally, seasonality is expected to follow changes in precession and obliquity orbital parameters. The combination of these two parameters in a normalized forcing record[10] suggests a maximum forcing at 11 ka (increased seasonality) and a minimum at 25 ka (reduced seasonality) with a smooth transition between extremes. The $\delta^{18}O$ record of Eagle Cave shows relative minimum $\delta^{18}O$ values during both periods and a lack of smooth transitions. Therefore, although this effect should not be considered negligible there is no evidence of its impact on the $\delta^{18}O$ record.

Most of the rainfall received over the Iberian Peninsula has a moisture source in the North Atlantic[11]. The moisture pools are related to ocean surface conditions[12], and they would be displaced not only with changing wind regimes but with modifications of ocean current dynamics[13]. A significant parameter to be considered is the sea-ice cover during winter, which prevents the uptake of moisture in the ocean from higher latitudes. Thus, periods with increased sea-ice cover, typical of reduced AMOC (Atlantic Meridional Overturning Circulation)[14], imply a biased moisture uptake towards lower latitudes in the North Atlantic which surface ocean waters have higher $\delta^{18}O$ values[15]. The high values of Eagle Cave $\delta^{18}O$ record during the glacial times in comparison to the Early Holocene are in agreement with the effects expected from the described modification of the moisture source. The highest isotope values are recorded during the Heinrich events H2 and H3, which is in agreement with extended sea-ice cover during these periods[16]. Therefore, this factor could have a significant impact in the Eagle Cave $\delta^{18}O$ record. However, lack of isotopic response in Eagle Cave speleothems during the Heinrich event H1, when AMOC circulation was drastically reduced affecting sea surface conditions[14,17] suggests that moisture source effect is limited in comparison with the control due to the amount of rainfall.

The modification of the ocean surface isotope composition ($\delta^{18}Osw$) is important to explain the speleothem records variability[18]. During the last 33 ka, the volumetric changes in continental glaciers and the relative sea level were severe[19], influencing the isotope composition of the surface of the ocean[20]. Therefore, the speleothem carbonate has been corrected for the ice volume effect according to sea level changes[21] considering a rate of change of 0.06‰/10 m of sea level[22]. This correction shifts the isotope signal towards higher isotope values during lower relative sea levels and makes it possible to compare the speleothem $\delta^{18}O$ signal during different periods regardless the changes in the global continental ice volume.

The stalagmites EA1 and EA4 are composed of both aragonite and calcite minerals. The isotope fractionation between water and these two carbonates differ by 0.6-0.78‰ for

the temperature range 0-30 ºC[7,23]. Carbonates with higher content of aragonite provide higher $\delta^{18}O$ values in Eagle Cave stalagmites (Fig. S5). The percentage of aragonite during most of the record is <17% and therefore isotope ratio variability related to different mineralogy is within uncertainty in oxygen isotope determinations. During Heinrich events H2 and H3 aragonite dominates the carbonate mineralogy. These periods record higher $\delta^{18}O$ values in the order of 1.4‰, which implies that the mineralogical factor explain only part of this isotope anomalies. In speleothems recording both minerals, occurrence of aragonite is considered an indicator of dry conditions[24]. The occurrence of periods with aragonite as dominating carbonate in Eagle Cave speleothems as an indicator of dry periods is in agreement with regional paleoclimate reconstructions[8,9]. Thus, the positive oxygen isotope anomalies recorded during Heinrich events H2 and H3 result mostly from the cumulative effects of different mineral fractionation, amount of precipitation and likely the source of precipitation.

Several factors affect the oxygen isotope composition of Eagle Cave record. Some of these controls can be corrected ($\delta^{18}Osw$) or considered to affect just some sectors of the speleothem (mineralogy), whereas other controls are considered negligible or do not seems to impact significantly the record (temperature and seasonality). After evaluation of the possible factors affecting the $\delta^{18}O$ signal in Eagle Cave speleothems, we consider that most of the variability in the record seems to be dominated by the amount of rainfall with the source of precipitation potentially playing a secondary but significant role in controlling the isotope signal.

References

1. Pedraza, J. & López, J. *Gredos, geología y glaciarismo*. (Obra social de la Caja de Ahorros de Ávila, Ávila, 1980).
2. Pedraza, J. & Fernández, P. in *Mapa geológico de Bohoyo, hoja 577, Serie MAGANA* (eds. Ruiz, P. & Gabaldón V.) 5-18 (IGME, Madrid, 1981).
3. Pedraza, J., Carrasco, R.M., Domínguez-Villar, D. & Villa, J. Late Pleistocene glacial evolutionary stages in the Gredos mountains (Iberian Central System). *Quat. Int.*, in press.
4. Pedraza, J. in *Geomorfología de España,* (ed. Gutierrez Elorza, M.) 63-100 (Rueda, 1994).
5. Hendy, C.H. The isotopic geochemistry of speleothems - I. The calculation of the effects of different modes of formation on the composition of speleothems and their applicability as paleoclimatic indicators. *Geochim. Comochim. Acta* **35**, 801-824 (1971).
6. Kim, S.T. & O'Neil, J.R. Equilibrium and nonequilibrium oxygen isotope effects in synthetic carbonates. *Geochim. Comochim. Acta* **61**, 3461-3475 (1997)
7. Kim, S.T., O'Neil, J.R., Hillaire-Marcel, C. & Mucci, A. Oxygen isotope fractionation between synthetic aragonite and water: influence of temperature and Mg^{2+} concentration. *Geochim. Comochim. Acta* **71**, 4704-4715 (2007).
8. Sánchez-Goñi, M.F. *et al.* Contrasting impacts of Dangaard-Oeschger events over a western European latitudinal transect modulated by orbital parameters. *Quat. Sci. Rev.* **27**, 1136-1151 (2008).
9. Fletcher, W.J. & Sánchez-Goñi, M.F. Orbital- and sub-orbital-scale climate impacts on vegetation of the western Mediterranean basin over the last 48,000 yr. *Quat. Res.* **70**, 451-464 (2008).

10. Huybers, P. Combined obliquity and precession pacing of late Pleistocene deglaciations. *Nature* **480**, 229-232 (2011).
11. Jorba, O., Pérez, C., Rocadenbosch, F. & Baldasano, J.M. Cluster analysis of 4-day back trajectories arriving in the Barcelona area, Spain, from 1997 to 2002. *J. Appli. Meteorol.* **43**, 887-901 (2004).
12. Gimeno L. *et al*. On the origin of continental precipitation. *Geophys. Res. Lett.* **37**, L13804 (2010).
13. Woollings, T., Gregory, J.M., Pinto, J.G., Reyers, M. & Brayshaw, D.J. Response of the North Atlantic storm track to climate change shaped by ocean-atmosphere coupling. *Nature-Geosci.* **5**, 313-317. (2012).
14. Denton G.H. *et al.* The Last Glacial Termination. *Science* **328**, 1652-1656 (2010).
15. Schmidt, G.A. Forward modeling of carbonate proxy data from planktonic foraminifera using oxygen isotope tracers in a global ocean model. *Paleoceanography* **14**, 482-497 (1999).
16. Grousset, F.E. *et al.* Patterns of ice-rafted detritus in the glacial North Atlantic (40-55ºN). *Paleoceanography* **8**, 175-192 (1993).
17. McManus, J.F., Francois, R., Gherardi, J.M., Keigwin, L.D. & Brown-Leger, S. Collapse and rapid resumption of Atalatic meridional circulation linked to deglacial climate changes. *Nature* **428**, 834-837 (2004).
18. Domínguez-Villar, D. *et al.* Oxygen isotope precipitation anomaly in the North Atlantic region during the 8.2 ka event. *Geology* **37**, 1095-1098 (2009).
19. Clark, P.U. *et al.* The last Glacial Maximum. *Science* **325**, 710-714 (2009).
20. Waelbroeck, C. *et al.* Sea-level and deep water temperature changes derived from benthic foraminifera isotopic records. *Quat. Sci. Rev.* **21**, 295-305 (2002).
21. Peltier, W.R. & Fairbanks, R.G. Global glacial ice volume and Last Glacial Maximum duration from an extended Barbados sea level record. *Quat. Sci. Rev.* **25**, 3322-3337 (2006).
22. Schrag, D.P. *et al.* The oxygen isotopic composition of seawater during the Last Glacial Maximum. *Quat. Sci. Rev.* **21**, 331-342 (2002).
23. Tarutani, T., Clayton, R.N. & Mayeda, T.K. Effect of polymorphism and magnesium substitution on oxygen isotope fractionation between calcium carbonate and water. *Geochim. Comochim. Acta* **33**, 987-996 (1969)
24. McMillan, E., Fairchild, I.J., Frisia, S., Borsato, A. & McDermott, F. Annual trace element cycles in calcite-aragonite speleothems: evidence of drought in the western Mediterranean 1200-1100 yr BP. *J. Quat. Sci.* **20**, 423-433 (2005).
25. Vieira, G. Combined numerical and geomorphological reconstructio of the Serra da Estrela plateau icefield, Portugal. *Geomorphology* **97**, 190-207 (2008).
26. Palacios, D., de Marcos, J. & Vázquez-Selem, L. Last Glacial Maximum and deglaciation of Sierra de Gredos, central Iberian Peninsula. *Quat. Int.* **233**, 16-26 (2011).
27. Palacios, D., Andrés, N., de Marcos, J. & Vázquez-Selem, L. Maximum glacial advance and deglaciation of the Pinar Valley (Sierra de Gredos, central Spain) and its significance in the Mediterranean context. *Geomorphology*, in press.
28. Palacios, D., de Andrés, N., de Marcos, J. & Vázquez-Selem, L. Glacial landforms and their paleoclimatic significance in Sierra de Guadarrama, Central Iberian Península. *Geomorphology* **139-140**, 67-78 (2012).
29. Gómez-Ortiz, A., Palacios, D., Palade, B., Vázquez-Selem, L. & Salvador-Franch, F. The deglaciation of the Sierra Nevada (southern Spain). *Geomorphology* **159-160**, 93-105 (2012).

30. Rodríguez-Rodríguez, L., Jiménez-Sánchez, M., Domínguez-Cuesta, M.J., Rico, M.T. & Valero-Garcés, B. Last deglaciation in northwestern Spain: new chronological and geomorphologic evidence from the Sanabria region. *Geomorphology* **135**, 48-65 (2011).
31. Vegas, J. Caracterización de eventos climáticos del Pleistoceno superior-Holoceno mediante el estudio sedimentológico de la laguna Grande (Sierra de Neila, NO Sistema Ibérico). *Rev. Soc. Geol. Esp.* **20**, 53-70 (2007).
32. Jalut G. *et al.* Glacial to interglacial vegetation changes in the northern and southern Pyrenees: deglaciation, vegetation cover and chronology. *Quat. Sci. Rev.* **11**, 449-480 (1992).
33. Reille, M. & Andrieu, V. The late Pleistocene and Holocene in the Lourdes Basin, western Pyrenees, France: new pollen analytical and chronological data. *Veget. Hist. Archaeobot.* **4**, 1-21 (1995).
34. Lewis, C., McDonald, E.V., Sancho, C., Peña, J.L. & Rhodes, E.J. Climatic implications of correlated upper Pleistocene glacial and fluvial deposits on the Cinca and Gállego rivers (NE Spain) based on OSL dating and soil stratigraphy. *Global and Planet. Change* **67**, 141-152 (2009).
35. González-Sampériz, P. *et al.* Climate variability in the Spanish Pyrenees during the last 30,000 yr revelaed by the El Portalet sequence. *Quat. Res.* **66**, 38-52 (2006).
36. Pallàs, R. *et al.* Late Pleistocene and Holocene glaciation in the Pyrenees: a critical review and new evidence from ^{10}Be exposure ages, south-central Pyrenees. *Quat. Sci. Rev.* **25**, 2937-2963 (2006).
37. Pallàs, R. *et al.* Small, isolated glacial catchments as priority targets for cosmogenic surface exposure dating of Pleistocene climate fluctuations, southeastern Pyrenees. *Geology* **38**, 891-894 (2010).
38. Delmas, M., Gunnell, Y., Braucher, R., Calvet, M. & Bourlès, D. Exposure age chronology of the last glaciation in the eastern Pyrenees. *Quat. Res.* **69**, 231-241 (2008).
39. Delmas, M. thesis, Paris University 1 (2009).
40. Delmas, M., Calvet, M., Gunnell, Y., Braucher, R. & Bourlès, D. Palaeogeography and ^{10}Be exposure-age chronology of middle and late Pleistocene glacier systems in the northern Pyrenees: implications for reconstructing regional palaeoclimates. *Palaeogeog. Palaeocliamt. Palaeoecol.* **305**, 109-122 (2011).
41. Federici, P.R. *et al.* Last Glacial Maximum and the Gschnitz stadial in the Maritime Alps according to ^{10}Be cosmogenic dating. *Boreas* **41**, 277-291 (2012).
42. Gianotti, F., Forno, M.G., Ivy-Ochs, S. & Kubik, P.W. New chronological and stratigraphical data on the Ivrea amphitheatre (Piedemont, NW Italy). *Quat. Int.* **190**, 123-135 (2008).
43. Bini, A. Stratigraphy, chronology and Palaeogeography of Quaternary deposits of the area between the Ticino and Olorsa rivers (Italy-Switzerland). *Geologia Insubrica* **2**, 21-46 (1997).
44. Ferraro, F.Age, sedimentation, and soil formation in the Val Sorda loess sequence, Northern Italy. *Quat. Int.* **204**, 54-64 (2009).
45. Monegato, G. *et al.* Evidence of a two-fold glacial advance during the last glacial maximum in the Tagliamento end moraine system (eastern Alps). *Quat. Res.* **68**, 284-302 (2007).
46. Giraudi, C. & Frezzotti, M. Late Pleistocene glacial events in the central Apennines, Italy. *Quat. Res.* **48**, 280-290 (1997).
47. Giraudi, C. The Campo Felice late Pleistocene glaciation (Apennines, central Italy). *J. Quat. Sci.* **27**, 432-440 (2012).

48. Hughes, P.D., Woodward, J.C., Van Calsteren, P.C. & Thomas, L.E. The glacial history of the Dinaric Alps, Montenegro. *Quat. Sci. Rev.* **30**, 3393-3412 (2011).
49. Lewin, J., Macklin, M.G., Woodward, J.C. Late Quaternary fluvial sedimentation in the voidomatis basin, Epirus, Northwest Greece. *Quat. Res.* **35**, 103-115 (1991).
50. Zhano, C., Akçar, N., Kubik, P.W. & Schlüchter, C. Chronology of Late Pleistocene glacier variations at the Uludağ Mountain, NW Turkey. *Quat. Sci. Rev.* **29**, 1173-1187 (2010).
51. Zhano, C., Akçar, N., Yavuz, V., Kubik, P.W. & Schlüchter, C. Surface exposure dating of late Pleistocene glaciations at the Dedegöl Mountains (Lake Beyşehir, SW Turkey). *J. Quat. Sci.* **24**, 1016-1028 (2009).
52. Sarıkaya, M.A., Zreda, M., Çiner, A. & Zweck, C. Cold and wet Last Glacial Maximum on Mountain Sandıras, SW Turkey, inferred from cosmogenic dating and glacier modeling. *Quat. Sci. Rev.* **27**, 769-780 (2008).
53. Sarıkaya, M.A., Zreda, M. & Çiner, A. Glaciations and paleoclimatic variations on Mount Erciyes, central Turkey, since Last Glacial Maximum, inferred from ^{36}Cl cosmgenic dating and glacier modeling. *Quat. Sci. Rev.* **28**, 2326-2341 (2009).
54. Akçar, N. *et al.* Paleoglacial records from Kavron Valley, NE Turkey: field and cosmogenic exposure dating evidence. *Quat. Int.* **164-165**, 170-183 (2007).
55. Akçar, N. *et al.* A case for a downwasting mountain glacier during Termination I, Verçenik valley, northeastern Turkey. *J. Quat. Sci.* **23**, 273-285 (2008).
56. Rodés, A. thesis, Barcelona University (2008).
57. Lifton, N.A. *et al.* Addressing solar modulation and long-term uncertainties in scaling secondary cosmic rays for in situ cosmogenic nuclide applications. *Earth Planet. Sci. Lett.* **239**, 140-161 (2005).
58. Balco, G., Stone, J.O., Lifton, N.A. & Dunai, T.J. A complete and easily accessible means of calculating surface exposure ages or erosion rates from ^{10}Be and ^{26}Al measurements. *Quaternary Geochronology* **3**, 174-195 (2008).
59. Cheng, H. *et al.* The half-lives of uranium-234 and thorium-230. *Chem. Geol.* **169**, 17-33 (2000).

Figures

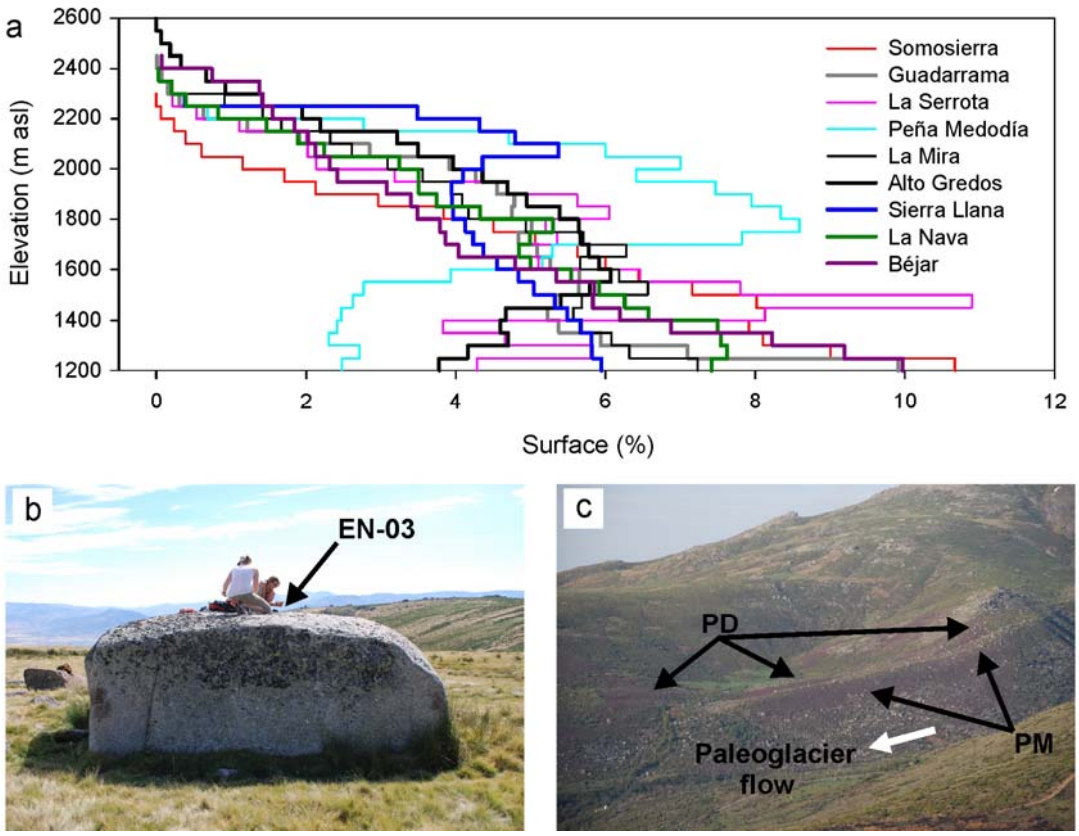

Fig. S1. Sampling of boulders from the PD unit in the Spanish Central System. (a) Plot showing the percentage of terrain above 1200 m asl for different massifs. The existence of plateaus and shelves favours the preservation of complete glacier deposit sequences. (b) Typical large erratic boulder at the GME stage without signs of rotation. The code sample of the ^{10}Be date is shown, see table S2. (c) Example showing PM and PD units in the right lateral moraine of El Duque paleoglacier in Béjar Range. Note the large dimensions of PM in comparison with PD.

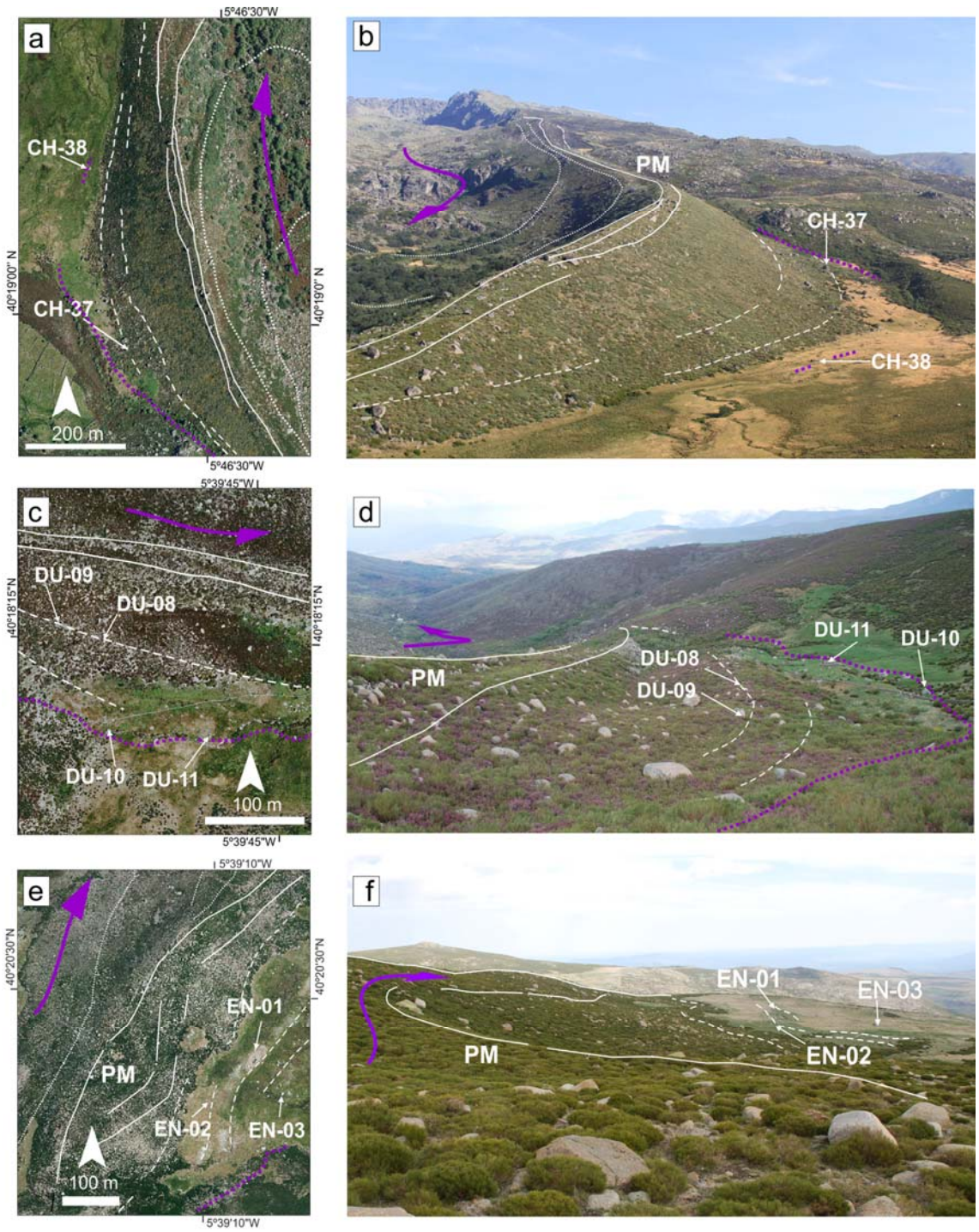

Fig. S2. Bejar Range maps and pictures showing the main geomorphic features identified around the sampling sites. For wider context within the paleoglaciers see Fig. 1. The maps represent the edge of the paleoglaciers reconstructed from erratic boulders (dotted purple line) and the moraine crests or boulders-belts from the PD unit (dashed white lines), PM unit (continuous white lines) and the geomorphic features from the recessional units (dotted white lines). Note that all maps are oriented to the North (white arrow tip) and have a scale bar, although oblique pictures have different orientations. Paleoglacier flow (purple arrow) is shown in most of the images for clarification. Sampled boulders are identified with the same code as in table S2. (a, b) Cuerpo de Hombre paleoglacier orthophoto and oblique picture. (c, d) Duque paleoglacier orthophoto and oblique picture. (e, f) Endrinal paleoglacier orthophoto and oblique picture. The orthophotos to construct the maps are from the free access database of the IGN (www.ign.es).

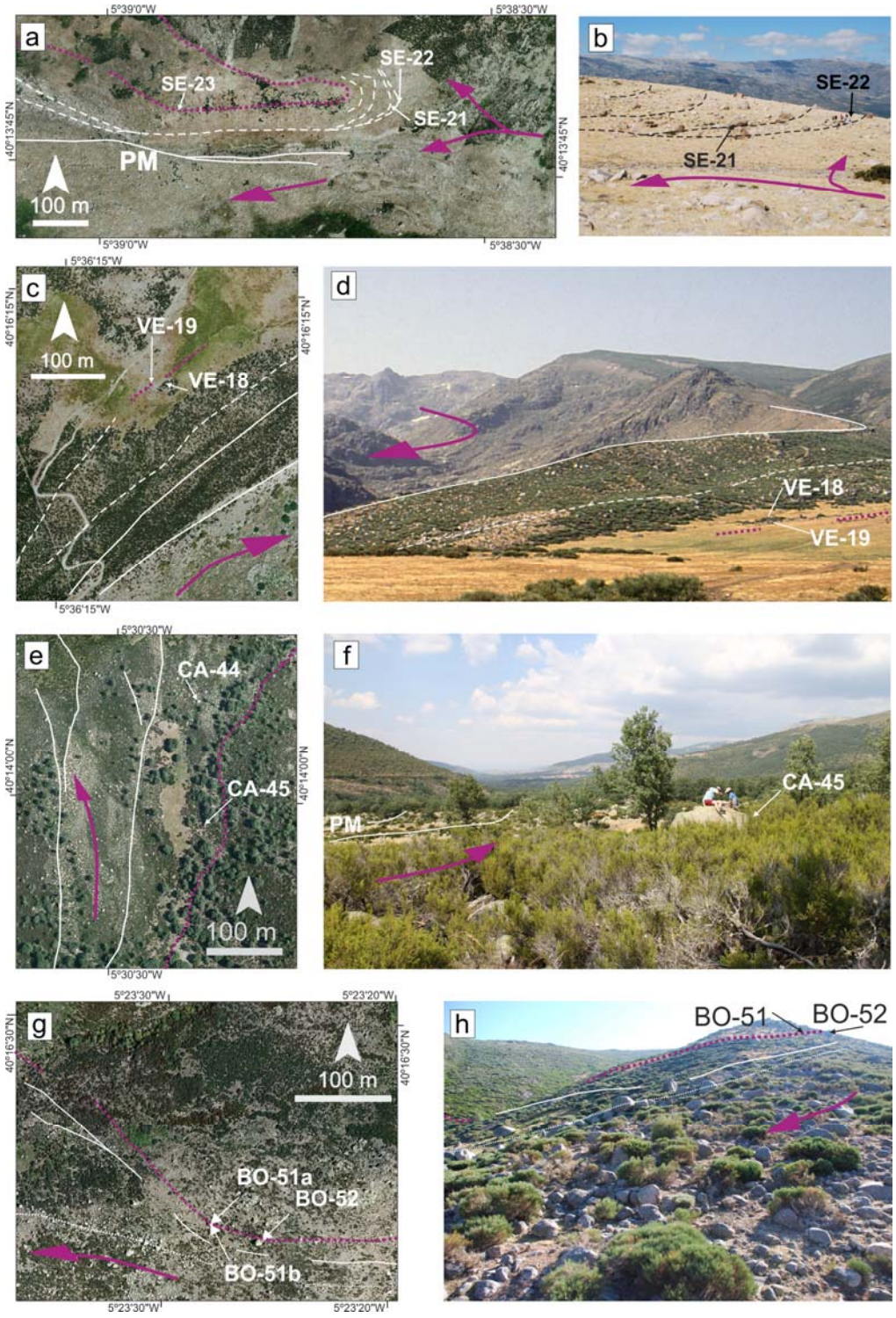

Fig. S3. Gredos Range maps and pictures showing the main geomorphic features identified around the sampling sites. For wider context within the paleoglaciers see Fig. 1. The maps represent the edge of the paleoglaciers reconstructed from erratic boulders (dotted purple line) and the moraine crests or boulders-belts from the PD unit (dashed white/black lines), PM unit (continuous white lines) and the geomorphic features from the recessional units (dotted white lines). Note that all maps are oriented to the North (white arrow tip) and have a scale bar, although oblique pictures have different orientations. Paleoglacier flow (purple arrow) is shown in the images for clarification. Note that a north arrow and a scale are shown in every map. Sampled boulders are identified with the same code as in table S2. (a, b) Serrá paleoglacier orthophoto and oblique picture. (c, d) Vega paleoglacier orthophoto and oblique picture. (e, f) Caballeros paleoglacier orthophoto and oblique picture. (g, h) Bohoyo orthophoto and oblique picture. The orthophotos to construct the maps are from the free access database of the IGN (www.ign.es).

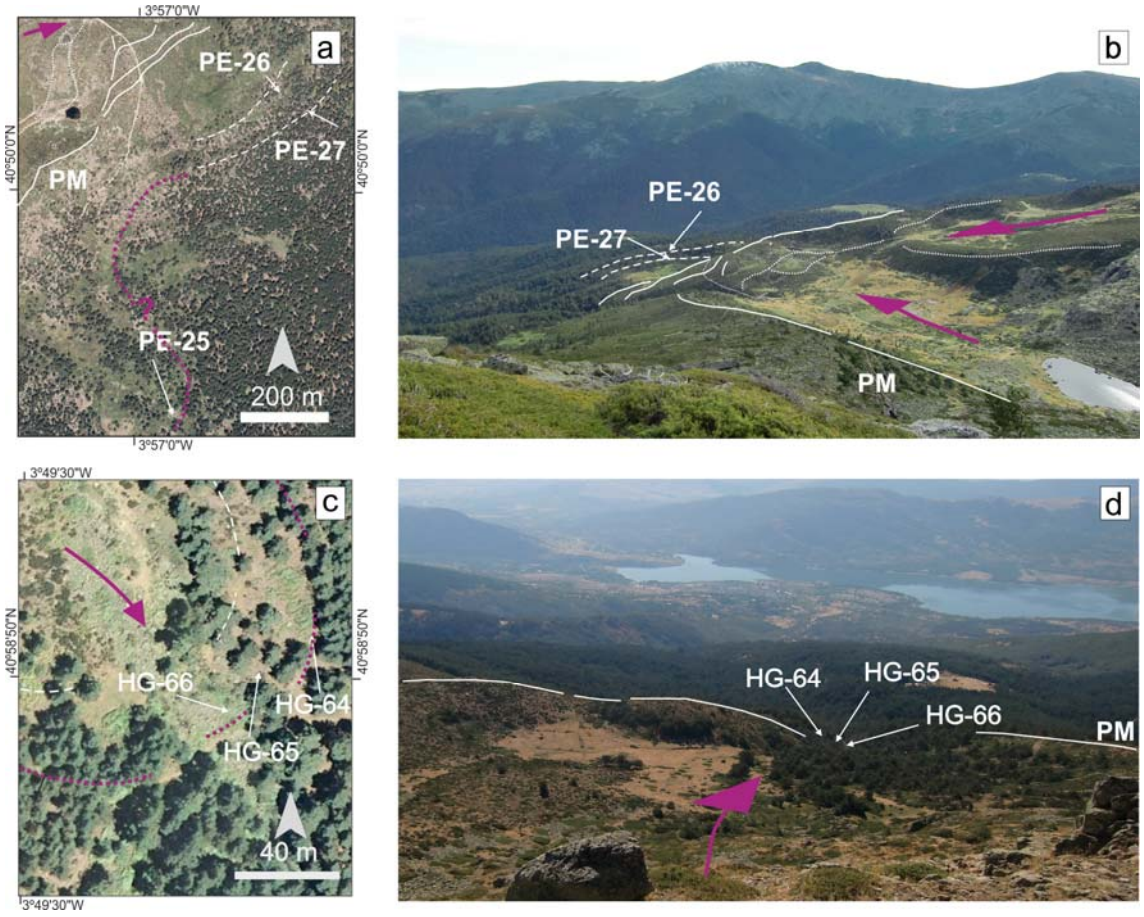

Fig. S4. Guadarrama Range maps and pictures showing the main geomorphic features identified around the sampling sites. For wider context within the paleoglaciers see Fig. 1. The maps represent the edge of the paleoglaciers reconstructed from erratic boulders (dotted purple line) and the moraine crests or boulders-belts from the PD unit (dashed white lines), PM unit (continuous white lines) and the geomorphic features from the recessional units (dotted white lines). Note that all maps are oriented to the North (white arrow tip) and have a scale bar, although oblique pictures have different orientations. Paleoglacier flow (purple arrow) is shown in the images for clarification. Sampled boulders are identified with the same code as in table S2. (a, b) Peñalara paleoglacier orthophoto and oblique picture. (c, d) Hoyo Grande paleoglacier orthophoto and oblique picture. The orthophotos to construct the maps are from the free access database of the IGN (www.ign.es).

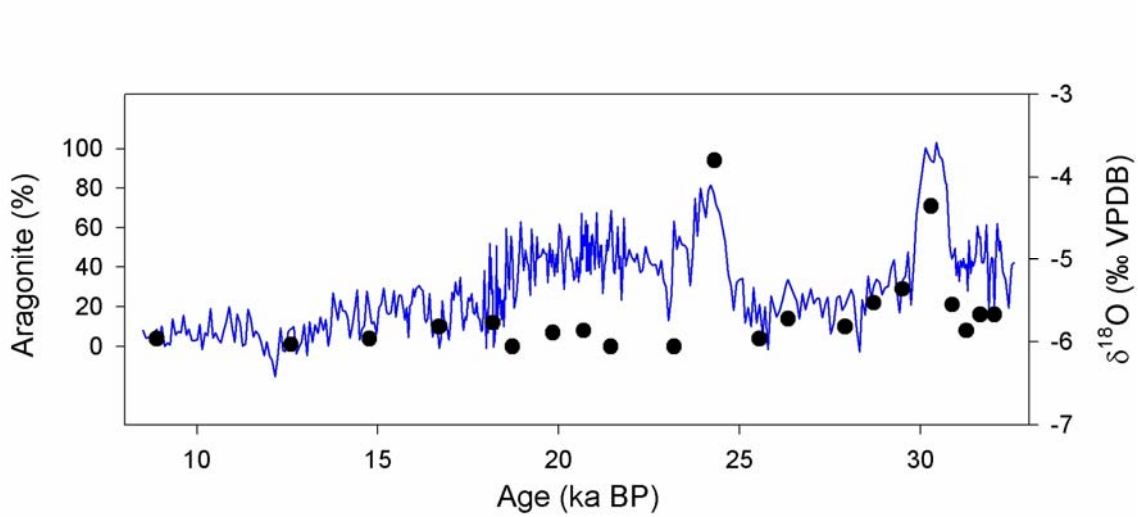

Fig. S5. Eagle Cave $\delta^{18}O$ record (blue line) with the percentage of aragonite in speleothem carbonate along EA1 and EA4 samples (black dots).

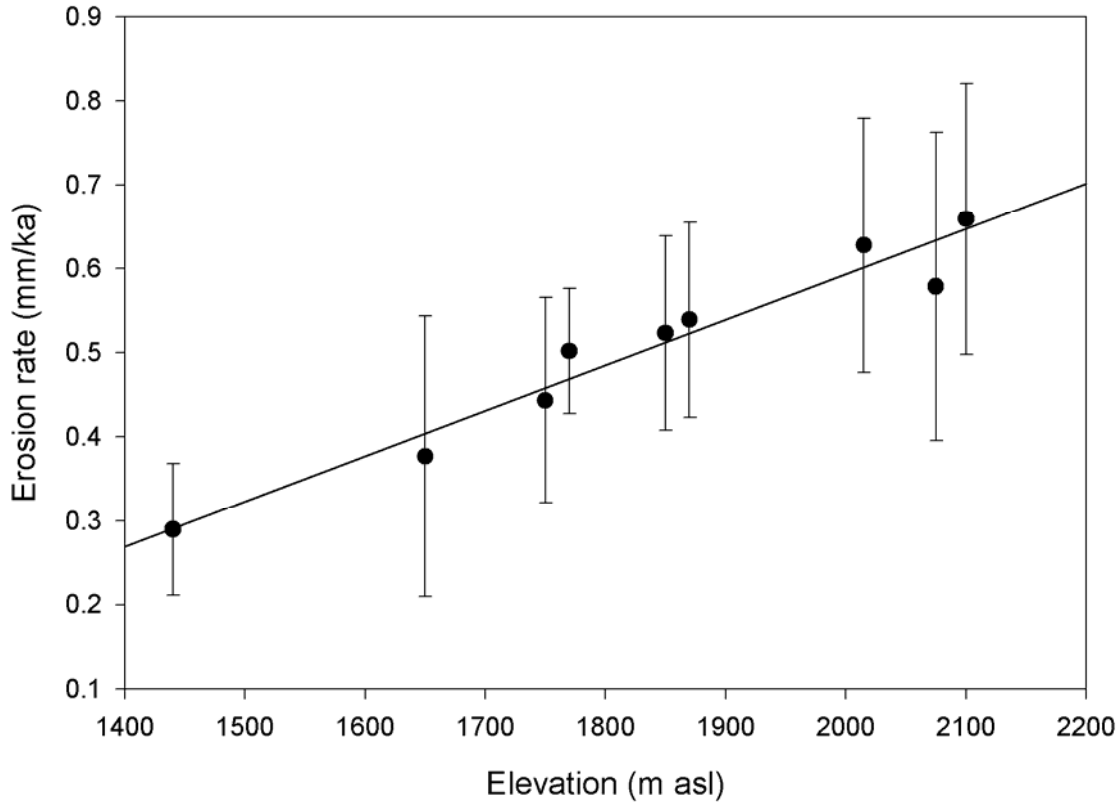

Fig. S6. Relationship between erosion rate and elevation of the measured sites in mountains from central Spain.

Table S1. Evaluation of chronologies for the glacier maximum extent in the Mediterranean region during the last glacial period. The list is a non exhaustive compilation of most significant or regionally relevant studies. The Iberian Central System is overrepresented in relation to other Mediterranean massifs to allow comparison of proximal sites to this study. Chronologies are considered robust (in bold) if they satisfy five criteria. Acc.: the accuracy of the method was controlled/corrected and no significant bias is expected; Rep.: the dates for this stage are replicated within uncertainties; GME: the provided date corresponds exactly with geomorphic indicators of the GME and there are no doubts about its identification; GC: the dated sequence is coherent within the geomorphologic context; PC: the chronology for the maximum extent of the glacier is coherent with regional paleoclimate. Dates are reported with their uncertainties unless a time range is reported, in which case an hyphen is used between maximum and minimum ages. Different stages around the maximum extension of glaciers are split with a slash. The chronologies of studies in which several dates are reported for the same stage lacking a synthetic age are reported as single dates separated by semicolons.

Site	Ref.	Dating technique	Age/s for GME (ka/ ka BP / cal ka BP)	Acc.	Rep.	GME	GC	PC
Iberian Massifs								
Serra da Estrela	25	TL	33.1±5.0; 30±4.5	N	?	?	Y	Y
Gredos valley	26	^{36}Cl	25.2±1.2; 24.2±0.9	N	?	N	Y	Y
Pinar valley	27	^{36}Cl	23.2±1.3; 22.3±1.6	N	?	N	Y	Y
Guadarrama	28	^{36}Cl	31.8±0.9	N	N	N	Y	Y
Sª Nevada	29	^{36}Cl	30.0±1.1; 19.6±0.8; 19.0±1.0	N	N	N	Y	Y
Sanabria	30	^{14}C	>26.0-25.2; 22.2-21.5	?	N	N	Y	Y
Sierra de Neila	31	^{14}C	>21.0-19.9	?	N	N	Y	Y
Pyrenees								
Multiple sites	32	^{14}C	>44.1-24.6	N	N	N	Y	N
Lourdes	33	^{14}C	>24.3-23.6	?	N	N	Y	Y
Gallego/Cinca	34	OSL	85±5 / 64±11 / 36±3 / 20±3	N	Y	Y	Y	N
Portalet	35	^{14}C	>33.8-32.2 / 23.4-17.0	N	N	N	N	Y
Ribagorza	36*	^{10}Be & ^{14}C	22.6±4.7; 19.2±2.0; 27.3-24.9; 22.6-21.1	Y	?	N	Y	Y
Malniu	37	^{10}Be	76.5±2.0; 49.2±1.3 / 23.9±0.6-21.3±0.6	Y	N	Y	Y	N
Têt	38**	^{10}Be	22.0±3.6 / 21.1±3.1	Y	Y	N	Y	Y
Carol	39	^{10}Be	22.9±2.7; 22.1±3.4; 21.7±2.8	Y	Y	N	Y	Y
Ariège	40	^{10}Be	81.4±14.6; 34.9±3.4	Y	N	Y	Y	N
Southern Alps								
Maritime Alps	41	^{10}Be	20.1±1.1	Y	?	N	Y	Y
Ivrea	42	^{10}Be	32.4±4.0; 27.9±3.1 / 20.8±1.5	Y	N	N	Y	Y
Verbano/Lario	43	^{14}C	22.4-21.6; 21.8-20.7	N	Y	N	Y	Y
Val Sorda	44	IRSL	18.7±2.1	?	N	?	Y	Y
Tagliamento	45	^{14}C	**26.5-23 / 24-21**	Y	Y	Y	Y	Y
Apennines								
Gran Sasso	46	^{14}C & Tephras	**28.9-24.9 / 24.9-20.5**	Y	Y	Y	Y	Y
Campo Felice	47	^{14}C & Tephra	27.5-26.2 / 23.2-22.1 / 19.5-18.9	N	N	Y	Y	Y
Balkans/Greece								
Montenegro	48	U-Th	>13.4±0.3	N	N	N	N	N
Mnt. Pindus	49	TL/ESR	28.0±7.1-24.3±2.6 / 19.6±3.0	N	N	-	Y	Y
Turkey								
Mnt. Uludağ	50	^{10}Be	**20.3±1.5**	Y	Y	Y	Y	Y
Dedegöl Mts.	51	^{10}Be	24.3±1.8	Y	N	N	Y	Y
Mnt Sandıras	52	^{36}Cl	**20.4±1.3 / 19.6±1.6**	Y	Y	Y	Y	Y
Mnt Erciyes	53	^{36}Cl	**21.3±0.9**	Y	Y	Y	Y	Y
Kavron valley	54***	^{10}Be	**21.5±1.6**	Y	Y	Y	Y	Y
Verçenik valley	55***	^{10}Be	21.77±1.6	Y	N	Y	Y	Y

Y:Yes; N: No; ?: Not enough information to evaluate; -: Not applicable. * modified according to Rodés[56], ** modified according to Delmas[39], *** modified according to Zhano *et al*.[50].

Table S2. ^{10}Be determinations and calculated exposure ages for boulders from PD unit in Béjar, Gredos and Guadarrama ranges.

Sample code	Latitude (dd)	Longitude (dd)	Altitude (m asl)	^{10}Be (10^3 at/g)	Sample thickness (cm)	Exposure age (ka BP)** [ε=0 cm·a^{-1}]	Modelled erosion rate (cm·a^{-1})	Exposure age (ka BP)** [ε=modelled]
EN-01	40.34073	5.65175	1859	338775 ±15343	5	18.9 ±2.1	0.00004422	**19.0 ±2.1**
EN-02	40.33987	5.65273	1865	341575 ±16707	5	18.9 ±2.1	0.00004452	**19.1 ±2.1**
EN-03	40.34005	5.65111	1853	477408 ±15254	2.5	26.5 ±2.8	0.00004387	**26.7 ±2.8**
DU-08	40.30414	5.66465	1450	292076 ±11683	2.5	21.8 ±2.3	0.00002377	**21.9 ±2.4**
DU-09	40.30430	5.66522	1460	276104 ±11044	3	20.5 ±2.2	0.00002427	**20.6 ±2.2**
DU-10	40.30335	5.66457	1436	336701 ±10101	5	27.0 ±2.8	0.00002302	**27.1 ±2.8**
DU-11	40.30333	5.66339	1426	260369 ±29649	2	20.3 ±3.1	0.00002257	**20.3 ±3.1**
VE-18	40.26973	5.60252	1607	342894 ±10250	5*	22.5 ±2.3	0.00003162	**22.6 ±2.4**
VE-19	40.26973	5.60252	1608	312877 ±27207	4	21.1 ±2.8	0.00003167	**21.2 ±2.8**
SE-21	40.23027	5.64377	1845	405369 ±10371	3*	21.9 ±2.2	0.00004412	**22.1 ±2.3**
SE-22	40.23030	5.64360	1843	400830 ±7466	5	22.1 ±2.2	0.00004342	**22.3 ±2.3**
SE-23	40.23007	5.64836	1862	423356 ±7287	5	23.3 ±2.4	0.00004437	**23.5 ±2.4**
PE-25	40.82868	3.94896	1758	125439 ±9125	4	7.8 ±0.9	0.00004482	**7.8 ±0.9**
PE-26	40.83500	3.94540	1828	345871 ±6311	2	19.7 ±2.0	0.00004267	**19.9 ±2.0**
PE-27	40.83536	3.94611	1840	335459 ±7625	3.5	18.7 ±1.9	0.00004327	**18.8 ±1.9**
CH-37	40.31615	5.77697	1555	310108 ±6202	5*	21.5 ±2.2	0.00002902	**21.6 ±2.2**
CH-38	40.31940	5.77798	1503	310108 ±6202	2*	23.0 ±2.3	0.00002642	**23.1 ±2.4**
CA-44	40.23454	5.50705	1295	282030 ±5919	3*	24.5 ±2.5	0.00001602	**24.6 ±2.5**
CA-45	40.23305	5.50689	1329	287155 ±4922	3*	24.5 ±2.5	0.00001767	**24.6 ±2.5**
BO-51a	40.27308	5.39108	1687	437679 ±23560	3*	27.6 ±3.1	0.00003562	**27.8 ±3.2**
BO-51b	40.27308	5.39108	1687	435133 ±16288	3*	26.7 ± 2.8	0.00003562	**26.9 ±2.9**
BO-52	40.27292	5.39049	1704	345193 ±10824	3*	21.6 ±2.3	0.00003647	**21.8 ±2.3**
HG-64	40.98071	3.82365	1801	376952 ±11578	4*	21.6 ±2.2	0.00004147	**21.7 ±2.3**
HG-65	40.98059	3.82389	1779	285164±7976	4*	17.3 ±1.8	0.00004127	**17.4 ±1.8**
HG-66	40.98044	3.82403	1793	384507 ±15152	5*	22.7 ±2.4	0.00004092	**22.9 ±2.5**

dd: decimal degrees; m asl: metres above sea level; Sample density is 2.7 g·cm^{-3} unless indicated by * which account for 2.65g·cm^{-3}. BP: before present, where "present" is considered the year 1950 AD; ε= erosion rate; ** scaling scheme according to Lifton *et al.*[57], external uncertainty is considered. Age calculation uses CRONUS-Earth v.2.2[58] and 07KNSTD standarization was used.

Table S3. Dates used for the age model of EA1 and EA4 speleothems

Sample ID	Distance from base (mm)	Weight (g)	^{238}U (ppb)	^{232}Th (ppt)	δ^{234}U meas.	[^{230}Th/^{238}U] activity	[^{230}Th/^{232}Th] atomic ratio (ppm)	Age corrected (yrs BP)*
EA4-11	684 ±2.0	0.1071	691.4 ±1.7	0 ±6	142.7 ±2.5	0.10875 ±0.00104	$8.3*10^6$ $\pm3.6*10^8$	**10,816 ±112**
EA4-21	648 ±2.0	0.1151	2277.7 ±6.1	0 ±6	130.3 ±2.5	0.13245 ±0.00062	$5.2*10^9$ $\pm3.4*10^{13}$	**13,489 ±75**
EA4-10	582 ±2.0	0.1361	1124.1 ±2.9	6 ±5	176.1 ±2.5	0.15894 ±0.00110	$5.3*10^5$ $\pm4.9*10^5$	**15,705 ±122**
EA4-29	531 ±2.0	0.0954	4506.9 ±16.2	0 ±7	148.8 ±3.5	0.17596 ±0.00087	$2.7*10^7$ $\pm4.3*10^8$	**17,991 ±114**
EA4-4	468 ±2.0	0.2138	353.8 ±0.9	69 ±3	-152.3 ±2.2	0.13245 ±0.00131	11206 ±543	**18,540 ±210**
EA4-18	376 ±2.0	0.1459	4037.4 ±15.9	188 ±5	120.3 ±2.6	0.19403 ±0.00103	68756 ±1783	**20,591 ±131**
EA4-9	325 ±2.0	0.1152	635.9 ±1.7	0 ±6	107.0 ±3.2	0.19420 ±0.00162	$1.1*10^9$ $\pm3.5*10^{12}$	**20,892 ±203**
EA4-17	298 ±2.0	0.1037	39.5 ±0.1	0 ±7	124.2 ±6.2	0.20569 ±0.00540	$2.8*10^8$ $\pm4.1*10^{12}$	**21,876 ±650**
EA1-4	674 ±2.5	0.1274	743.4 ±1.8	59 ±5	49.1 ±2.3	0.21161 ±0.00135	44265 ±4146	**24,441 ±186**
EA1-6	595 ±1.5	0.0867	1145.8 ±2.7	5 ±8	56.9 ±2.5	0.26037 ±0.00130	$9.6*10^5$ $\pm1.5*10^6$	**30,676 ±197**
EA1-8	555 ±2.5	0.1051	193.2 ±0.4	6 ±7	37.4 ±3.5	0.26652 ±0.00216	$1.4*10^5$ $\pm1.5*10^5$	**32,234 ±332**

*Age determination uses decay constants by Cheng *et al.*[59]. Age corrections were calculated using an average crustal ^{230}Th/^{232}Th atomic ratio of $4.4\cdot10^{-6}$ ± $2.2\cdot10^{-6}$. Those are the values for a material at secular equilibrium, with the crustal ^{232}Th/^{238}U value of 3.8. The errors are arbitrarily assumed to be 50%. B.P. stands for "Before Present" where the "Present" is defined as the year 1950 A.D. Age model was calculated using a linear interpolation between dates. The growth rate at the base of EA4 (below the sample EA4-17) was obtained by transferring the date of the sample EA1-4 into EA4 age model after matching of the δ^{18}O stratigraphy of both stalagmites. The analytical error associated to the dates is considered a minimum absolute error estimate.